# Colliding-Droplet Microreactor: Rapid On-Demand Inertial Mixing and Metal-Catalyzed Aqueous Phase Oxidation Processes

Ryan D. Davis,[†] Michael I. Jacobs,[†,‡] Frances A. Houle,[†] and Kevin R. Wilson*,[†]

[†]Chemical Sciences Division, Lawrence Berkeley National Laboratory, Berkeley, California 94720, United States
[‡]Department of Chemistry, University of California, Berkeley, California 94720, United States

S Supporting Information

ABSTRACT: In-depth investigations of the kinetics of aqueous chemistry occurring in microdroplet environments require experimental techniques that allow a reaction to be initiated at a well-defined point in time and space. Merging microdroplets of different reactants is one such approach. The mixing dynamics of unconfined (airborne) microdroplets have yet to be studied in detail, which is an essential step toward widespread use and application of merged droplet microreactors for monitoring chemical reactions. Here, we present an on-demand experimental approach for initiating chemical reactions in and characterizing the mixing dynamics of colliding airborne microdroplets (40 ± 5 μm diameter) using a streak-based fluorescence microscopy technique. The advantages of this approach include the ability to generate two well-controlled monodisperse microdroplet streams and collide (and thus mix) the microdroplets with high spatial and temporal control while consuming small amounts of sample (<0.1 μL/s). Mixing times are influenced not only by the velocity at which microdroplets collide but also the geometry of the collision (i.e., head-on vs off-center collision). For head-on collisions, we achieve submillisecond mixing times ranging from ~900 μs at a collision velocity of 0.1 m/s to <200 μs at ~6 m/s. For low-velocity (<1 m/s) off-center collisions, mixing times were consistent with the head-on cases. For high-velocity (i.e., > 1 m/s) off-center collisions, mixing times increased by as much as a factor of 6 (e.g., at ~6 m/s, mixing times increased from <200 μs for head-on collisions to ~1200 μs for highly off-center collisions). At collision velocities >7 m/s, droplet separation and fragmentation occurred, resulting in incomplete mixing. These results suggest a limited range of collision velocities over which complete and rapid mixing can be achieved when using airborne merged microdroplets to, e.g., study reaction kinetics when reaction times are short relative to typical bulk reactor mixing times. We benchmark our reactor using an aqueous-phase oxidation reaction: iron-catalyzed hydroxyl radical production from hydrogen peroxide (Fenton's reaction) and subsequent aqueous-phase oxidation of organic species in solution. Kinetic simulations of our measurements show that quantitative agreement can be obtained using known bulk-phase kinetics for bimolecular reactions in our colliding-droplet microreactor.
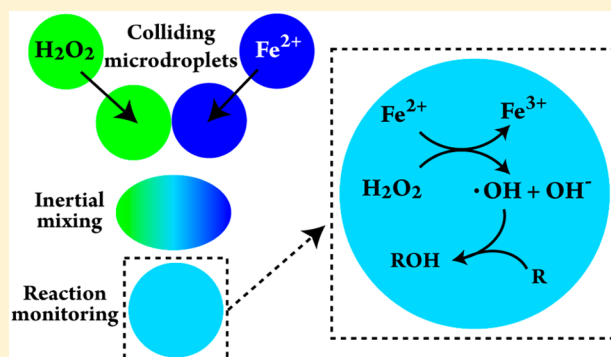
T here is a fundamental interest in chemistry occurring in microenvironments such as emulsions, microdroplets, and at interfaces.[1−8] This interest has been driven by the ubiquitous presence of microenvironments throughout nature (e.g., atmospheric aerosols, biologic cells, geologic pores) as well as economic and sustainability initiatives to reduce costs by using small sample sizes.[1−8] Recently, interest in microenvironment chemistry has increased following reports that reactions occurring in microenvironments can be enhanced relative to in bulk. This enhancement is proposed to be as a result of, e.g., interfacial effects.[2−6] However, a fundamental understanding of microenvironment properties has remained elusive, and it is unclear to what extent they may influence processes occurring in nature in, e.g., cloud droplets.[2] Thus, further studies are of value, particularly studies of airborne microdroplets. Traditional droplet-based microfluidic devices are powerful tools for studying microenvironments, but the confinement of material within and in contact with microfluidic channel walls and the need for a carrier fluid can limit their applicability.[1,7,8]

In an effort to expand microfluidic applications beyond the constraints of channel walls, airborne merged-droplet techniques for studying reaction dynamics have been developed in which drop(let)s of different compositions collide in air and inertially mix (i.e., mixing is facilitated by convection stimulated by the inertia of the colliding droplets[9]). These have been largely based on crossed electrospray plumes,[4] where the droplet collision process is not well controlled and microdroplets are highly charged, and on ultrasonic levitation,[8] where drops are large (i.e., μL volumes) relative to the sizes pertinent to, e.g., cloud droplets or aerosols (pL to <aL volumes),[10] and mixing time scales are long (seconds) relative to the fast mixing

necessary to detect many transient reactive intermediates (microseconds or less),[11] which can provide crucial information about reaction dynamics. Thus, although elegant and powerful techniques in their own right, the aforementioned merged-droplet reactors may have limited applicability. Furthermore, the inertial mixing dynamics of airborne colliding microdroplets have not been well characterized. This may limit their utility, particularly for aqueous systems, where the air−water interface is expected to play a crucial role in reaction kinetics.[2,12]

Aqueous-phase chemistry in microdroplets is of particular interest in multiple fields. For example, in synthetic "green" chemistry, water as a benign solvent is appealing because of the low environmental impact. However, many synthetic reactions exhibit slow bulk aqueous kinetics.[2,13] Thus, the observation that reactions can be accelerated in microdroplets has led to speculation that microdroplet synthesis may be a route to overcoming these kinetic limitations.[2] In the atmosphere, water is a primary component of atmospheric aerosols and cloud/fog droplets, and aqueous chemical processes occurring in these particles are an important source of organic particulate matter.[10,14] However, a mechanistic understanding of some key aqueous processes is lacking.[10,14] Iron-catalyzed production of reactive oxygen species from hydrogen peroxide (H_2O_2) (Fenton's reaction), which is a particularly intriguing reaction due to its widespread relevance from a cellular level (e.g., cellular oxidation catalyzed by iron-containing heme)[15] to large scale applications in wastewater treatment,[16] is one example where a fundamental understanding remains elusive. Bulk reaction rates may not fully capture the reaction dynamics of Fenton's chemistry in microdroplets where interfacial effects may dominate due to the high surface-to-volume ratio.[12]

Here, we present the design and characterization of an on-demand colliding-droplet microreactor, where two streams of microdroplets of different composition collide in a gaseous medium, utilizing inertial mixing to rapidly initiate a chemical reaction at a well-defined point in time and space. In this setup, which is a variation of the droplet collision approaches with pressurized fluid reservoirs (i.e., not on-demand),[17,18] the size of colliding microdroplets ($40 \pm 5 \ \mu m$ diameter), collision geometry, collision relative velocity (0.01 to 8 m/s), and timing of the collision are well-controlled parameters. Ultimately, this colliding-droplet microreactor is to be a tool for studying aqueous chemical reactions of interest in, e.g., environmental and synthetic organic chemistry. However, in order to interpret the time evolution of a reaction, a prerequisite is an understanding of the inertial mixing dynamics of airborne microdroplets as they collide. Thus, the initial focus of this report is a characterization of the inertial mixing time using a novel streak-based fluorescence microscopy approach. We then show that kinetic data can be extracted using the colliding-droplet microreactor to study Fenton's chemistry.

■ EXPERIMENTAL SECTION

Approach. The inertial mixing dynamics and aqueous organic oxidation chemistry of colliding microdroplets in air is studied using an on-demand colliding-droplet streak-based fluorescence microscopy approach with a pulsed light-emitting diode (LED) as the excitation source to achieve high temporal resolution. For mixing dynamics, a stream of aqueous droplets of 125 μM Rhodamine B (RhB; 9-(2-carboxyphenyl)-6-diethylamino-3-xanthenylidene-diethylammonium chloride; Exciton) is merged with a separate stream of aqueous microdroplets composed of 20% (v/v) sulfuric acid (H_2SO_4; Sigma-

Aldrich), as demonstrated in Figure 1. RhB is a highly fluorescent dye with a fluorescence spectrum that is insensitive
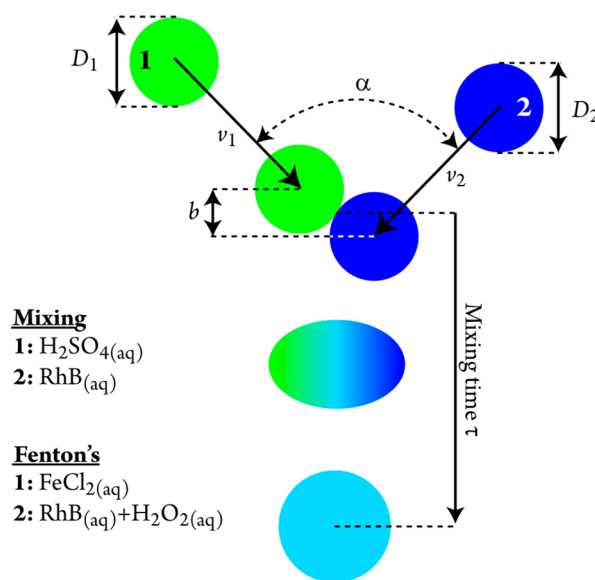

Figure 1. Experimental approach to studying inertial mixing and iron-catalyzed production of reactive oxygen species (Fenton's chemistry) in the colliding-droplet microreactor.

to pH changes above pH ≈ 6.[19] Below pH ≈ 6, the fluorescence intensity of RhB decreases with pH (see Figure S1). The extent of mixing between merged RhB + H_2SO_4 droplets is thus determined by monitoring the decrease in RhB fluorescence intensity (as a result of the abrupt decrease in pH) and the homogeneity of the fluorescence intensity distribution throughout the droplets. Fenton's chemistry in microdroplets is studied by colliding a droplet stream of aqueous iron(II) chloride ($FeCl_2$; Alfa-Aesar, ultra dry, 99.99% metals basis) with a stream of $RhB_{(aq)}$ droplets doped with H_2O_2 (Sigma-Aldrich, 35 wt % stock solution). The initial concentrations in the separate droplet streams are 125 μM RhB and 0.2 M (or 2 M) H_2O_2 in one droplet and 0.02 M (or 0.2 M) $FeCl_2$ in the other. Droplets are equally sized, so dilution upon mixing reduces concentrations by half. The reaction between Fe^{2+} and H_2O_2 generates hydroxyl radicals ($^\bullet OH$) which subsequently react with RhB forming a nonfluorescent product.[20] The reaction progress is monitored using the decay in RhB fluorescence intensity.

Droplet Collider. The experimental arrangement is shown in Figure 2. Droplets are generated from dual on-demand piezoelectric droplet dispensers with a 20 μm diameter orifice (Microfab). The dispensers are enclosed in a blackout box to minimize ambient light and air currents. Each dispenser is connected to individual fluid reservoirs that supply the aqueous solutions. The fluid reservoirs are vented syringes connected to the dispenser with polyethylene tubing and placed with a residual fluid level ~5 cm below the dispenser tip. The dispensers are driven by independently controlled square wave voltage pulses from a data acquisition card (DAQ; 0−10 V analog outputs) that are boosted by home-built 5 V/V voltage amplifiers. Droplets are generated with 14−18 V, 5−9 μs square wave pulses at a repetition rate of 2 kHz. Different combinations of these parameters generate droplets of comparable diameter with different exit velocities. Upon exiting the nozzle of the dispenser, droplets slow to their terminal
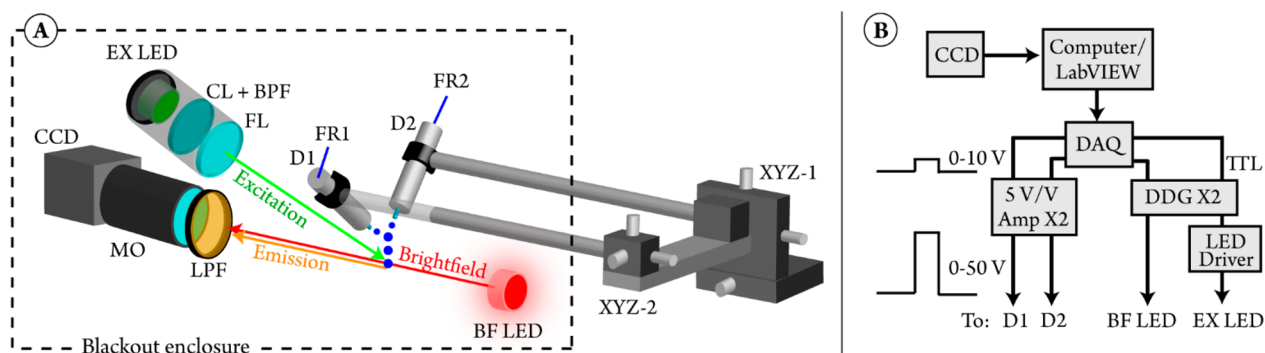
Figure 2. Experimental arrangement. (A) Optomechanical arrangement. BF LED: red brightfield LED; EX LED: excitation LED; CL: collimating lens; BPF: bandpass filter; FL: focusing lens; LPF: long-pass filter; MO: microscope objective; CCD: charge-coupled device camera; D1 and D2: droplet dispensers; FR1 and FR2: fluid reservoirs (vented 5 mL syringes); XYZ-1: translation stage for simultaneously positioning D1 and D2; XYZ-2: mini translation stage for independently positioning D1; (B) electrical control and data acquisition. DAQ: data acquisition card (with two 0−10 V analog outputs and two TTL triggers); DDG: digital delay generators; Amp: 5 V/V power amplifier.
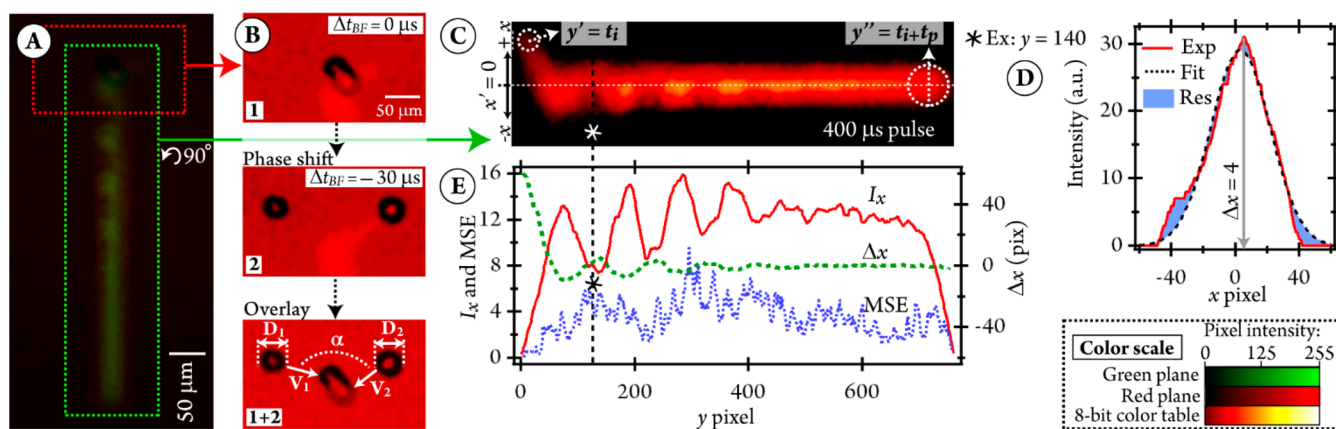

Figure 3. Overview of the image analysis. (A) A snapshot of fluorescence emission with simultaneous brightfield imaging. The 24-bit RGB image is processed to extract the 8-bit red plane (for brightfield) and 8-bit green plane (for fluorescence emission). (B) Determining the collision parameters from the brightfield images. Image 1 shows the initial point of collision ($\Delta t_{BF} = 0$), and image 2 shows the precollision droplet positions with a phase shift of $\Delta t_{BF} = -30$ μs. The information extracted from the images is shown on an overlay of images 1 and 2 (b, not shown for clarity, is also determined). (C) Shown here is a 400 μs pulse rotated 90°. Because the length of time of each excitation pulse is known and well-controlled, vertical (y) pixel values of the emission streak are indicators of time. (D) The horizontal (x) distribution of emission intensity is plotted for each row of pixels in the area-of-interest (AOI) and compared to a Gaussian fit, as demonstrated for $y = 140$. The average intensity of each row (I_x), Gaussian fit residual (Res) mean square error (MSE), and deviation of fluorescence intensity from merged-droplet center (Δx) are determined for each row (for the example at $y = 140$: $\Delta x = 4$, MSE = 5.4, and $I_x = 7.5$). (E) I_x, Δx, and MSE plotted as a function of vertical (y) AOI pixel for the emission streak shown.

velocity within several milliseconds. The collision velocity is thus controlled by varying the voltage pulse, the distance droplets travel before collision, and the collision angle (α) between dispensers.

To adjust the trajectories of the generated droplets and guiding collisions, the droplet dispensers are held in rotation-adjustable collars (to vary α, which is set to either 90 or 160°) and connected to rods that extend outside the blackout enclosure and are fixed to translation stages. One translation stage (XYZ-1) simultaneously positions both dispensers for alignment with optics and vertical tracking of reaction progress. Another stage independently positions a single dispenser to guide and control collisions (XYZ-2). The dispenser with the RhB solution is mounted to XYZ-2 so that changes to the droplet collision trajectory are observed in the fluorescence emission images without relying on brightfield images, as described in more detail in Image Analysis.

Imaging and Excitation Arrangement. The RhB fluorescence excitation source is a high-power LED (Thorlabs,

350 mW optical power, 538 nm peak wavelength; see Figure S2). The excitation LED is collimated, spectrally filtered with a bandpass filter (520 nm center wavelength, 40 nm fwhm), and then focused onto the droplets using a plano-convex lens (75 mm focal length). The focus of the excitation LED evenly illuminates the field-of-view of the imaging camera. Brightfield images are obtained by back-illuminating droplets with a red LED (Thorlabs, 630 nm). Droplet collisions and fluorescence emission are imaged onto a charge-coupled device (CCD) camera (Sentec STC-MC33USB or Thorlabs DCU224C) with a microscope objective and lens tube (either 1.5 or 8.2× total magnification) and a long-pass filter (550 nm cut-on wavelength; to prevent light from the excitation LED from being imaged). Typically, the CCD gain is set to its maximum value. The brightfield and excitation LED pulses are triggered at the same frequency as the droplet generators to create stable stroboscopic images. The LED pulse width and phase shift (i.e., timing relative to droplet generation) are controlled with independent digital delay generators (Stanford Research

Systems, Inc., DG535). Typical pulse widths are 1 μs for the brightfield LED and 400 μs for the excitation LED. Because droplet velocities are not constant (see, for example, Figure S3A), pulsing the excitation LED provides a well-defined temporal indicator for tracking droplet mixing and reaction dynamics.

Image Analysis. An overview of the image analysis procedure is shown in Figure 3. Images are collected and postprocessed in a custom LabVIEW program. An example of simultaneous brightfield and fluorescence imaging is shown in Figure 3A. Each pixel in the collected images contains three color values: red, green, and blue (RGB, 24-bit). The RGB color images are decomposed into separate 8-bit grayscale images by extracting the individual red and green color planes, thus isolating the fluorescence emission (green plane) from the brightfield (red plane). All of the collision parameters (i.e., the parameters shown in Figure 1) and inertial mixing time (τ) are determined from these isolated images. As shown in Figure 3B, the standard approach to analyzing brightfield images was used to determine the droplet diameters D_1 and D_2, droplet velocities v_1 and v_2, α, and the separation distance b between the centers of the colliding droplets by phase shifting the brightfield LED pulse by a length of time Δt_{BF} relative to the point of collision.[17,18] (See Supporting Information (SI), Expanded Experimental Detail of Brightfield Image Analysis for more details.) The relative collision velocity U is then calculated from eq 1

$$U^2 = v_1^2 + v_2^2 - 2v_1v_2\cos\alpha \tag{1}$$

and the impact parameter X is calculated from eq 2

$$X = 2b/(D_1 + D_2) \tag{2}$$

For the experiments reported here, $D_1 = D_2$ and $v_1 = v_2$.

Fluorescence emission is analyzed by extracting and isolating the green plane of the RGB image, as demonstrated in Figure 3C. The length of the excitation LED pulses (t_p, 400 μs) is such that droplets travel a long distance relative to their diameter while illuminated with the excitation LED. Thus, the RhB fluorescence appears on the camera as a streak. Each streak contains temporal and spatial information about the extent of droplet mixing. Merged droplets travel vertically (in the y-direction in the images). Thus, the y-axis of the images is converted to time using the known length of the excitation pulse.[21] The center position of the droplet at the beginning of the fluorescence streak (y') correlates with the initial time of the pulse (t_i), and the center position at the end of the fluorescence streak (y'') correlates with the final time ($t_i + t_p$) of the pulse (i.e., the time between y' and y'' is 400 μs). At 2 kHz (500 μs between sequential droplets), there is 100 μs between pulse streaks. The merged-droplet velocity is not constant as droplets slow to their terminal velocity (Figure S3A), and mixing times are not linearly related to the distance traveled. Thus, pulsed excitation, rather than continuous illumination, is used to provide a temporal marker of the evolution of fluorescence emission.

Spatial information about the distribution of RhB fluorescence intensity is obtained by analyzing the fluorescence streak area-of-interest (AOI) in the horizontal (x) plane of the images. The AOI center x-pixel value (x') is set to zero, where all values to the right of center are positive, and those to the left are negative. For uniformly mixed droplets, the fluorescence intensity distribution is observed to be Gaussian across the droplet with a horizontal cross section intensity maximum at x'.

For nonuniformly mixed droplets, the fluorescence intensity distribution deviates from this Gaussian profile, and the x-value of maximum fluorescence intensity (x_{max}) does not necessarily coincide with x'. Thus, to monitor mixing, for each row of x-pixels, the intensity is plotted as a function of x and fit to a Gaussian function, as demonstrated in Figure 3D. The distribution of the fluorescence intensity relative to x' (Δx) is expressed as eq 3

$$\Delta x = x_{max} - x' \tag{3}$$

where x_{max} is determined from the measured distribution. Δx provides one measure of the homogeneity of merged droplets. As another quantitative measure of droplet mixing, the variation in and extent of homogeneity of the fluorescence distribution is quantified here from the residual mean square error (MSE) of the Gaussian fit to the measured distribution. To further track mixing, the average x-intensity of each row (I_x) is used to monitor the fluorescence intensity as a function of y (and thus time). Figure 3E shows Δx, MSE, and I_x plotted as a function of y for the fluorescence emission streak shown. This image analysis approach to determining mixing is conceptually similar to those applied elsewhere,[8,9] except our approach is applied to a streak rather than an instantaneous snapshot of a singular mixing event.

For mixing experiments, τ is determined as when Δx and MSE reach stable minimum values, and I_x decays to e^{-1} of its initial value (this decay in I_x does not occur in the absence of H_2SO_4, as shown in Figure S3B with pure water droplets). Variations in I_x, such as seen in Figure 3E, that arise due to droplet rotation or shape oscillations, do not result in stable values of I_x and will therefore not result in underestimations in τ. A separate calibration curve of RhB fluorescence intensity vs concentration, shown in Figure S4, is used to directly compare the experimental microdroplet results of the Fenton-initiated oxidation of RhB to kinetic simulations.

Statistical Analysis. Uncertainty in τ is reported as ± 1 SD of individual τ determinations from at least 5 collected image frames. (At a droplet generation rate of 2 kHz, an imaging rate of 30 Hz, and an exposure time of ~30 ms, each collected image represented the time-average of ~60 individual collision events. Thus, 5 collected image frames represented ~300 individual collision events.) Uncertainty in U and X are limited by the resolution of the imaging systems (~4.9 μm/pix at 1.5× and ~0.9 μm/pix at 8.2× magnification, as determined by target calibration), and thus typically ~$\pm$ 0.1 for X and ~$\pm$ 0.02 m/s for U (as described in Image Analysis).

Kinetic Simulations. Stochastic kinetic simulations are performed to compare our results of Fenton-initiated aqueous organic oxidation chemistry in microdroplets to that of bulk predictions using the open-access Kinetiscope software package (v. 1.1.743).[22] Reactions are simulated with 10^7 particles at constant environmental conditions using literature rate constants and assuming that the merged droplet is a single homogeneous compartment.

■ RESULTS AND DISCUSSION

Inertial Mixing. *Microdroplet Mixing at Low Velocity.* The results from a droplet mixing experiment at low relative velocity ($U = 0.21 \pm 0.02$ m/s) are shown in Figure 4 for two different impact parameters. As seen in Figure 4A, images of the fluorescence intensity streaks appear similar for both head-on ($X = 0$) and off-center ($X = 0.8$) collisions. Within the first 400 μs pulse, there are, however, small differences in the
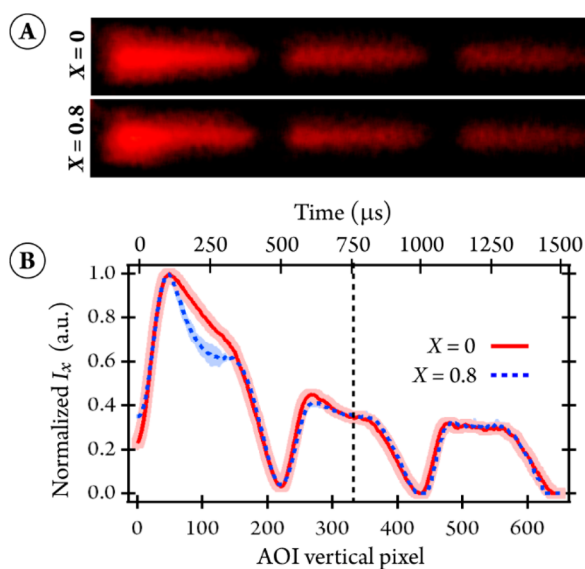
Figure 4. Mixing of 125 μM RhB$_{(aq)}$ microdroplets with 20% H$_2$SO$_4$ microdroplets at low velocity ($U = 0.21 \pm 0.02$ m/s) for impact parameters $X = 0.0 \pm 0.1$ and 0.8 ± 0.1. (A) Snapshots of emission streaks. (B) Plot of I_x vs y (time). The shaded areas represent ± 1 SD of 20 collected images. The dashed line indicates the approximate value of τ (750 $\pm$ 50 and 760 $\pm$ 50 μs for $X = 0$ and 0.8, respectively).

distribution of fluorescence intensity with the merged droplets, as evident in the plots of I_x and Δx.

For head-on collisions, I_x (shown normalized in Figure 4B) decreases smoothly from the moment of impact ($t = 0$) until reaching a steady value of $I_x \approx 0.35$ at $t \approx 750$ μs. Also, for head-on collisions, Δx (Figure S5A) shows that the fluorescence intensity is initially negatively displaced (i.e., left of the merged-droplet center, in the direction the premerged RhB droplet had been traveling, consistent with inertial considerations) and then gradually becomes centrally distributed at $t \approx 750$ μs. MSE (Figure S5B) also reaches a minimum at $t \approx 750$ μs. All three parameters (I_x, Δx, and MSE) reach their steady-state minimum values, which indicate a homogeneously mixed droplet, and thus τ. For this experiment, and all experiments reported here, τ coincided with the time at which I_x decayed to e^{-1} ($\sim$37%) of its original value, with τ well-approximated from the e-folding time of I_x. Here, for head-on collisions, $\tau = 750 \pm 50$ μs.

For the off-center collision ($X = 0.8$) shown in Figure 4, I_x decreases nonuniformly, i.e., I_x initially decreases rapidly and then briefly levels off before the final decrease to a steady value. Despite this oscillatory behavior in I_x for the off-center collision, a steady value of $\approx$0.35 is reached at the same time as for head-on collisions ($\sim$750 μs). Similarly, Δx reaches a steady value at $\sim$750 μs, although Δx for the off-center collision reaches a more negative value after the collision (because for higher X, less of each droplet comes in to contact at the initial moment of collision, and each individual droplet center of mass continues on its original trajectory less impeded than for head-on collisions).[23,24] Notably, I_x, Δx, and MSE all converge to minimum values at approximately the same time as for head-on collisions, with a determined value for the off-center collision of $\tau = 760 \pm 50$ μs. Thus, for this case ($U = 0.21$ m/s), $\tau(X = 0) \approx \tau(X = 0.8)$, suggesting that the collision impact parameter has a negligible effect on τ at low U.

Microdroplet Mixing at High Velocity. While the results shown in Figure 4 indicate that τ is insensitive to X for the lowest range of relative velocities studied here, there is a notably different behavior for mixing at significantly higher U, as demonstrated in Figure 5 for $U = 3.7 \pm 0.1$ m/s. As seen in
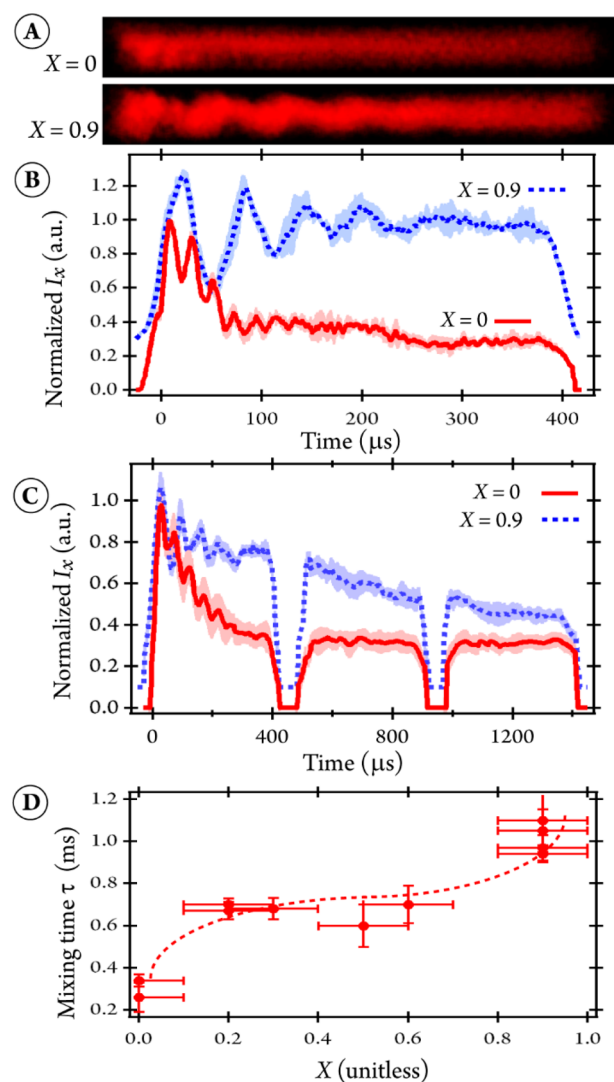

Figure 5. Mixing of 125 μM RhB$_{(aq)}$ microdroplets with 20% H$_2$SO$_4$ microdroplets at high velocity ($U = 3.7 \pm 0.1$ m/s) at different X. (A) Snapshots of emission streaks for $X = 0.0 \pm 0.1$ and 0.9 ± 0.1. (B) Plot of I_x vs time for $X = 0.0 \pm 0.1$ and 0.9 ± 0.1 (8.2$\times$ magnification, first 400 μs pulse). The plot for $X = 0.9$ is offset vertically by 0.3 I_x. Shaded error shows ± 1 SD of 20 processed images. (C) Plot of I_x vs time for $X = 0.0 \pm 0.1$ and 0.9 ± 0.1 (1.5$\times$ magnification). The plot for $X = 0.9$ is offset vertically by 0.1 I_x. (D) Plot of τ as a function of X for $U = 3.7 \pm 0.1$ m/s.

Figure 5A, the emission streaks for different values of X exhibit different intensity distributions, with nonuniformities more evident as X increases. (To show details of the time following the initial collision, only the first 400 μs streaks are shown here.) As seen in Figure 5B, the evolution of I_x over time is correspondingly different for the different values of X. For the head-on collision ($X = 0$), I_x decreases rapidly, with $\tau = 260$ μs, and there is an underlying oscillation with a period of $\sim$20 μs that is particularly pronounced during the first 100 μs following the collision. This oscillation period is consistent with the linear

oscillation frequencies of droplet coalescence[25] (see SI, Estimated Linear Oscillation Frequencies). These initial oscillations in I_x for $X = 0$ are thus likely a result of droplet shape oscillations, as seen in the brightfield images shown in Figure S6A. Variations in I_x due to droplet shape oscillations do not result in stable values of I_x and will therefore not result in underestimations in τ but may represent the lower limit of determined τ values.

For off-center collisions ($X = 0.9$), I_x decreases more gradually (i.e., complete mixing is not observed in the first pulse), and the rapid oscillations are not present or unresolvable. Rather, there are lower-frequency oscillations than those observed for the head-on case, with a period of ∼70−100 μs, likely due to droplet rotation, as shown in Figure S6B. Complete mixing in this case does not occur until long time scales ($\tau = 1.1 \pm 0.1$ ms for $X = 0.9$), as seen in Figure 5C, suggesting very different droplet−droplet collision dynamics for low and high values of X at high U.

As shown in Figure 5D, the different postcollision behaviors for different values of X (all at $U = 3.7 \pm 0.1$ m/s) result in a range of τ values. For a head-on collision, $\tau \approx 300$ μs, which is roughly 2.5 times faster than for $U = 0.2$ m/s. For moderately off-center collisions ($X = 0.2$ to 0.6), τ increases to ∼600 μs. As X increases further, τ continues to increase to ∼1 ms at $X = 0.9$, which is a longer mixing time than observed for the low-velocity example (0.2 m/s), demonstrating that the geometry of the collision influences droplet mixing times at high impact velocities.

Microdroplet Mixing Behavior from $U \approx 0.1$ to 8 m/s. Mixing experiments were performed across a wide range of U while adjusting the collision geometry (i.e., X). The complete range of results is shown in Figure 6 along with the convective
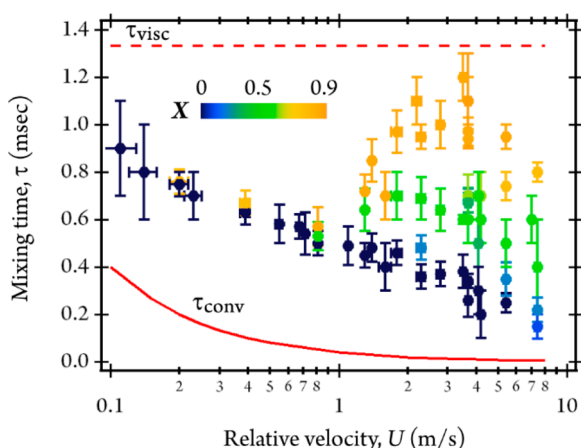

Figure 6. τ plotted as a function of U. Color coding denotes the value of X. Solid red line is τ_{conv} and dashed line is τ_{visc} (calculated with $\nu = 1.2 \times 10^{-6}$ m^2 s^{-1}) for 40 μm microdroplets.

time scale (τ_{conv}; the time to transport material one droplet length at a velocity equal to U, given by $\tau_{conv} = D/U$) and viscous diffusion time scale (τ_{visc}; the time required to diffuse momentum across the droplet length, given by $\tau_{visc} = D^2/\nu$, where ν is the fluid kinematic viscosity).

As seen in Figure 6, all values of τ lie between τ_{conv} and τ_{visc}. There is a clear distinction in mixing behavior not only as a function of U, but X, as well. At low velocities (∼0.1 to 0.9 m/s) τ decreases with U and the influence of X, if any, is not readily apparent. This decrease in τ is consistent with

expectations of increased convective mixing as U increases, as indicated in Figure 6, where the convective time scale is the lower limit to τ.[9] However, while τ does indeed continue to decrease for head-on collisions at higher U (>1 m/s), there is actually a clear *increase* in τ for off-center collisions at higher velocity. For example, at $U = 3.5 \pm 0.1$ m/s and $X = 0.9$, $\tau = 1.2 \pm 0.1$ ms, which is a larger value of τ than for the lowest velocity studied ($U = 0.11 \pm 0.02$ m/s, $\tau = 0.9 \pm 0.2$ ms), although still much shorter than diffusive mixing alone (∼4 s with an RhB diffusion coefficient of 4×10^{-10} m^{2}s^{-1}).[26] Above $U \approx 4$ m/s, τ decreases for all values of X, but there remains a clear separation between τ for head-on and off-center collisions. At the highest velocities studied ($U = 7.4 \pm 0.1$ m/s) droplet fragmentation and separation began to occur for head-on and highly off-center collisions, resulting in apparently unmixed droplet fragments (see Figure S7, for example, and SI, *Microdroplet Coalescence vs Separation*). These results demonstrate that knowledge of the collision geometry and outcome (e.g., permanent coalescence or separation) is important for understanding the extent of mixing in colliding microdroplets, particularly at high collision velocities.

Relating τ to Microdroplet Fluid Dynamics. While the initial trend in τ, where τ decreases with increasing U, is consistent with expectations of inertial mixing driven by convection, the reason for the subsequent increase in τ for off-center collisions is not readily apparent. Previous studies have shown that internal flow patterns in colliding droplets are related to collision geometry.[23,24] Simulations of internal fluid flow and mass transfer in high-velocity colliding off-center droplets have shown that the direction of fluid flow remains outward and is largely unidirectional (see SI, Additional Discussion of Relating τ to Microdroplet Fluid Dynamics).[24] We thus hypothesize that variations in internal flow patterns, and thus fluid mass transfer, due to differences in collision geometry are the source of the variation in τ with X at high velocity, as shown in Figure S6. However, at lower velocities, the rapid contraction of the liquid bridge (as seen in Figure S8) and high internal pressures of small microdroplets appears sufficient to stimulate internal flow patterns that mix droplets on submillisecond time scales regardless of X.

Although we speculate that differences in internal flow patterns are the driving force for the variation in τ with X, a quantitative description of how these internal flows influence mixing dynamics is beyond the scope of this article. However, to facilitate the applicability of merged-droplet on-demand techniques in chemical analysis, we use the nondimensional Weber number (We), which scales the relative importance of fluid inertia to surface tension and is a parameter commonly used to generalize droplet collision outcomes, to qualitatively constrain the conditions where collision geometry appears most important on mixing dynamics. These results are shown in Figure S9 and discussed in SI, Generalizations of Mixing Dynamics.

Comparisons and Extrapolations. The shortest τ reported here is ∼200 μs. This is an order of magnitude improvement over commercial stopped-flow mixing devices (∼2 ms)[27] and comparable to chaotic-advection microfluidic droplet mixers (where droplets are confined in microfluidic channels).[1] Continuous-flow microfluidic mixers have been reported which can achieve mixing times of ∼8 to 15 μs,[27,28] but the sample is confined in microfluidic channels, and more sample volume is typically consumed (e.g., 600 μL/s)[27] than is necessary for the colliding-droplet microreactor (<0.14 μL/s;

see SI, Sample Volume Consumption Rate). Ultrafast nanospray theta-capillary mixing times of ~1 μs have been reported,[11] although the electrospray process generates polydisperse droplets that are highly charged. Although these latter two techniques report faster mixing times, the simplicity, efficiency, and control with the on-demand colliding-droplet microreactor are advantages.

Of the colliding-droplet mixers reported to date that we are aware of, the fastest mixing times reported here are 4 orders of magnitude faster than those reported by Chainani et al.[8] (several seconds) using ultrasonically levitated drops and a factor of 3 improvement over the fastest mixing time reported by Carroll and Hidrovo[9] (600 μs) using colliding droplets (~100 μm diameter, ~ 0.5 m/s) confined in microfluidic channels. For specific values of U, our mixing times are consistent with recent reports that studied a limited range of microdroplet collision velocities.[29,30] Lee et al.[4] collided 13 $\pm$ 6 μm diameter electrosprayed microdroplets at 84 $\pm$ 18 m/s and estimated their mixing times to be less than a few μs, which is faster than reported here, although the high We number associated with those conditions ($We \approx 1000$) is well above the predicted separation threshold for colliding microdroplets of that size ($We \approx 32.5$).[24]

We estimate that mixing times comparable to ultrarapid continuous-flow microfluidic mixers (~10 to 20 μs) are possible by colliding 10 μm microdroplets at ~14 m/s (see Figure S10). The size-dependence of microdroplet mixing could be probed with the colliding-droplet microreactor by applying more complex waveforms to the droplet dispensers to achieve smaller droplet diameters.[31] However, as is, the range of mixing times reported here (<900 μs) are sufficiently rapid to study reaction kinetics, as demonstrated in Fenton's Chemistry in the Colliding-Droplet Microreactor.

Fenton's Chemistry in the Colliding-Droplet Microreactor. The goal of characterizing microdroplet mixing dynamics in the present study is to apply this experimental approach to the analysis of aqueous chemical reactions of interest in environmental and sustainable synthetic chemistry. Here, we use the microdroplet collider to study Fe^{2+}-catalyzed $^{\bullet}OH$ generation from H_2O_2 and subsequent reaction of RhB with $^{\bullet}OH$ (Fenton's chemistry). Having determined that reliable and repeatable mixing times are achieved at $U \approx 0.1$ to 1 m/s for our droplet size range and for all values of X, we chose to mix reactants at an impact velocity of $U \approx 0.5$ m/s. At this velocity, the mixing time is ~500−600 μs, which is close to the time between adjacent droplets in the train, and the postcollision velocity of falling droplets rapidly reaches terminal velocity (~0.1 m/s) and remains constant.

The kinetic results are shown in Figure 7 for two different reactant concentrations (0.01 M $FeCl_2$/0.1 M H_2O_2 and 0.1 M $FeCl_2$/1 M H_2O_2). The raw experimental data, from the point of collision to the point where the droplet stream exits the field-of-view, is shown in Figure 7A. There is a clear decrease in RhB fluorescence intensity along the propagation direction of the droplet stream. The initial decrease in I_x (first pulse, t = 0 to 400 μs) is attributable largely to dilution. As the droplet stream falls, the reaction progress continues, and I_x continues to decrease. This is attributable to the production of $^{\bullet}OH$ radicals that rapidly react with RhB to form a nonfluorescent product.[20] The reaction progress from the beginning of the second droplet emission pulse (t = 500 μs) is shown in Figure 7B with fluorescence intensity converted to concentration units.
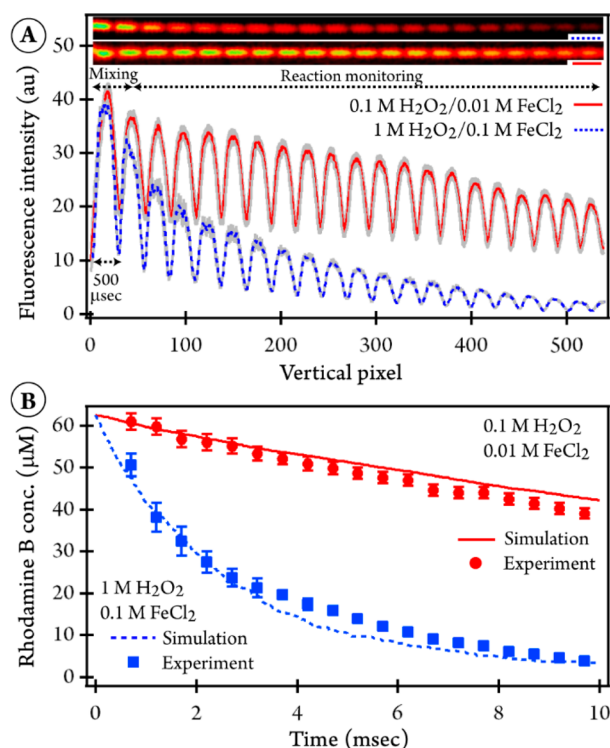

Figure 7. Experimental results of Fenton's chemistry in the colliding-droplet microreactor. (A) Image processing results (I_x vs vertical AOI pixel). The shaded portion of the plot shows ± 1 SD of 50 captured images. The inset images (top) show snapshots of the fluorescence emission streaks. (B) Experimentally observed decrease in RhB concentration as a function of time compared to predictions of stochastic kinetic simulations. Uncertainty is ± 1 SD of image processing of 50 captured images.

To test the validity of our approach toward studying metal-catalyzed reactions as well as more generalized chemistry, we simulated the evolution of the RhB concentration vs time using a stochastic kinetics simulator. The simulated reactions, including competing and product reactions, are shown in Table S1. The rate coefficients in the model are from the literature.[16,32] A range of rate coefficient values (50 to 76 M^{-1} s^{-1}) are reported for the initial reaction of Fe^{2+} + $H_2O_2 \rightarrow Fe^{3+}$ + OH^- + $^{\bullet}OH$.[12,16] In Figure 7B, we used a rate coefficient of 76 M^{-1} s^{-1} (Figure S11 shows the simulation with 50 M^{-1} s^{-1}). This model neglects surface processes and assumes that the chemical composition of the fused droplet is uniform. The experimental results compared to simulations are shown in Figure 7B.

As seen in Figure 7B, the experimental results of RhB degradation match the simulation predictions. The implication inherent in this observation is that for our microdroplet sizes (~50 μm diameter postmerging) any potential reaction acceleration due to, e.g., Fe^{2+} adsorbed to the air−water interface,[12] is not resolvable, and bulk rate coefficients are sufficient to explain our experimental results. Fallah-Araghi et al.[5] also did not quantify a reaction acceleration (imine synthesis) for emulsions ~50 μm diameter. This, however, does not negate the possibility of a quantifiable acceleration at smaller droplet sizes; the extent of reaction acceleration has been shown to be a function of compartment size ($1/D$) for a range of reactions.[2−5]

CONCLUSIONS

We presented an experimental approach to studying the mixing dynamics of and aqueous chemical reactions initiated in colliding airborne microdroplets using an on-demand colliding-droplet microreactor and a streak-based fluorescence microscopy analytical technique. The advantages of this technique include the ability to generate two well-controlled monodisperse droplet streams; merge droplets with high spatial and temporal control; achieve submillisecond inertial mixing times; and have low sample consumption during an experiment (<0.14 μL/s). Notably, we observed that inertial mixing times are influenced not only by the relative velocity at which droplets collide but also the geometry of the collision. This effect became most pronounced at higher collision relative velocities (>1 m/s, $We > 1$). At the highest relative velocities studied (>7 m/s, $We > 30$), droplet separation and fragmentation occurred, resulting in incomplete mixing. From these results, we identified a limited range of impact velocities over which complete and rapid mixing can be assumed when using airborne merged microdroplets. We note that our results may not be strictly valid for highly charged droplet plumes, such as in electrospray or for droplet sizes significantly different than used here (~40 μm diameter precoalescence). However, we do anticipate the phenomena to be rather general and that faster mixing times are possible for smaller droplet diameters (e.g., 20 μs for 10 μm microdroplets).

To demonstrate the general applicability of this technique, we studied Fenton's chemistry initiated in the merged microdroplets. The degradation of RhB in microdroplets was consistent with bulk predictions from $^\bullet$OH production. Although degradation products were not identified here, it was clear that reactive oxygen species were generated that reacted with the aromatic organic RhB, pointing toward the colliding-droplet microreactor as a technique to study aqueous organic chemistry in a wide range of chemical systems with millisecond reaction times. In the future, coupling of the colliding-droplet microreactor with mass spectral analysis will further increase the utility of this efficient on-demand technique.

ASSOCIATED CONTENT

Ⓢ Supporting Information

The Supporting Information is available free of charge on the ACS Publications website at DOI: 10.1021/acs.analchem.7b03601.

Supporting Information includes 11 supplemental figures, expanded experimental detail, and additional discussion (PDF)

AUTHOR INFORMATION

Corresponding Author

*E-mail: krwilson@lbl.gov; Tel: (510) 495-2474.

ORCID Ⓞ

Michael I. Jacobs: 0000-0003-3682-0409
Frances A. Houle: 0000-0001-5571-2548
Kevin R. Wilson: 0000-0003-0264-0872

Notes

The authors declare no competing financial interest.

REFERENCES

(1) Song, H.; Chen, D. L.; Ismagilov, R. F. *Angew. Chem., Int. Ed.* **2006**, *45*, 7336−7356.
(2) Banerjee, S.; Gnanamani, E.; Yan, X.; Zare, R. N. *Analyst* **2017**, *142*, 1399−1402.
(3) Girod, M.; Moyano, E.; Campbell, D.; Cooks, R. *Chem. Sci.* **2011**, *2*, 501−510.
(4) Lee, J.; Kim, S.; Nam, H.; Zare, R. *Proc. Natl. Acad. Sci. U. S. A.* **2015**, *112*, 3898−3903.
(5) Fallah-Araghi, A.; Meguellati, K.; Baret, J.-C.; Harrak, A.; Mangeat, T.; Karplus, M.; Ladame, S.; Marques, C.; Griffiths, A. *Phys. Rev. Lett.* [Online] **2014**, *112*.10.1103/PhysRevLett.112.028301
(6) Crawford, E.; Esen, C.; Volmer, D. *Anal. Chem.* **2016**, *88*, 8396−8403.
(7) Pierre, Z.; Field, C.; Scheeline, A. *Anal. Chem.* **2009**, *81*, 8496−8502.
(8) Chainani, E.; Choi, W.-H.; Ngo, K.; Scheeline, A. *Anal. Chem.* **2014**, *86*, 2229−2237.
(9) Carroll, B.; Hidrovo, C. *Heat Transfer Eng.* **2013**, *34*, 120−130.
(10) McNeill, V. F. *Environ. Sci. Technol.* **2015**, *49*, 1237−1244.
(11) Mortensen, D.; Williams, E. *J. Am. Chem. Soc.* **2016**, *138*, 3453−3460.
(12) Enami, S.; Sakamoto, Y.; Colussi, A. *Proc. Natl. Acad. Sci. U. S. A.* **2014**, *111*, 623−628.
(13) Li, C.-J. *Acc. Chem. Res.* **2010**, *43*, 581−590.
(14) Chu, B.; Liggio, J.; Liu, Y.; He, H.; Takekawa, H.; Li, S.-M.; Hao, J. *Sci. Rep.* **2017**, *7*, 40311.
(15) Rifkind, J.; Mohanty, J.; Nagababu, E. *Front. Physiol.* [Online] **2015**, *5*.10.3389/fphys.2014.00500
(16) Bokare, A.; Choi, W. *J. Hazard. Mater.* **2014**, *275*, 121−135.
(17) Gotaas, C.; Havelka, P.; Jakobsen, H.; Svendsen, H. *Phys. Fluids* **2007**, *19*, 102105.
(18) Planchette, C.; Lorenceau, E.; Brenn, G. *J. Fluid Mech.* **2012**, *702*, 5−25.
(19) Coppeta, J.; Rogers, C. *Exp. Fluids* **1998**, *25*, 1−15.
(20) Nidheesh, P. V.; Rajan, R. *RSC Adv.* **2016**, *6*, 5330−5340.
(21) Krishnan, R.; Saitoh, H.; Terada, H.; Centonze, V.; Herman, B. *Rev. Sci. Instrum.* **2003**, *74*, 2714−2721.
(22) Hinsberg, W. D.; Houle, F. A. *Kinetiscope*; Columbia Hill Technical Consulting: Fremont, CA, 2015; www.hinsberg.net/kinetiscope.
(23) Saroka, M. D.; Ashgriz, N.; Movassat, M. *J. Appl. Fluid Mech.* **2012**, *5*, 23.
(24) Saroka, M. D.; Ashgriz, N. *J. Fluids* **2015**, *2015*, 1−15.
(25) Bzdek, B. R.; Collard, L.; Sprittles, J. E.; Hudson, A. J.; Reid, J. P. *J. Chem. Phys.* **2016**, *145*, 054502.
(26) Fang, X.; Xuan, Y.; Li, Q. *Appl. Phys. Lett.* **2009**, *95*, 203108.
(27) Shastry, M.; Luck, S. D.; Roder, H. *Biophys. J.* **1998**, *74*, 2714−2721.
(28) Wu, L.; Lapidus, L. *Anal. Chem.* **2013**, *85*, 4920−4924.
(29) Jacobs, M. I.; Davies, J. F.; Lee, L.; Davis, R. D.; Houle, F. A.; Wilson, K. R. *Anal. Chem.* **2017**, DOI: 10.1021/acs.analchem.7b03704.
(30) Anahara, K.; Kohno, J. *J. Phys. Chem. B* **2017**, DOI: 10.1021/acs.jpcb.7b08526.
(31) Vaughn, B. S.; Tracey, P. J.; Trevitt, A. J. *RSC Adv.* **2016**, *6*, 60215−60222.
(32) Khalfaoui, N.; Boutoumi, H.; Khalaf, H.; Oturan, N.; Oturan, M. A. *Curr. Org. Chem.* **2012**, *16*, 2083−2090.